Silicon Dioxide Coating of Titanium Dioxide Nanoparticles from Dielectric Barrier Discharge in a Gaseous Mixture of Silane and Nitrogen

Sebastian Dahle, Lienhard Wegewitz, Fei Qi, Alfred P. Weber & Wolfgang Maus-Friedrichs

Plasma
Chemistry
and Plasma
Processing

🐎 Springer

🐎 Springer

Springer

ORIGINAL PAPER

Silicon Dioxide Coating of Titanium Dioxide Nanoparticles from Dielectric Barrier Discharge in a Gaseous Mixture of Silane and Nitrogen

Sebastian Dahle · Lienhard Wegewitz · Fei Qi · Alfred P. Weber · Wolfgang Maus-Friedrichs

Abstract The coating of titanium dioxide nanoparticles with silicon dioxide has been carried out by dielectric barrier discharge (DBD) plasma treatments to enhance the thermostability of Titania for applications at high temperature processes. During the first coating processing step, a closed film of silicon nitride was produced via plasma treatment in a gaseous mixture of silane and nitrogen, while atmospheric surface contaminations got mainly removed. In the second processing step, the DBD plasma treatment in oxygen or air was used to convert the silicon nitride mainly into silicon dioxide. Remaining carbon impurities at the interfaces between titanium dioxide and silicon nitride after the nitrogen/silane plasma treatment were subsequently removed simultaneously. Atomic force microscopy and X-ray photoelectron spectroscopy were employed to study the DBD plasma treatments of the TiO_2 nanoparticles.

Keywords X-ray photoelectron spectroscopy · Atomic force microscopy · Core–shell-structure

S. Dahle · L. Wegewitz · W. Maus-Friedrichs (✉)
Institut für Energieforschung und Physikalische Technologien, Technische Universität Clausthal, Leibnizstrasse 4, 38678 Clausthal-Zellerfeld, Germany
e-mail: w.maus-friedrichs@pe.tu-clausthal.de

S. Dahle
Fakultät für Naturwissenschaften und Technik, Hochschule für Angewandte Wissenschaft und Kunst, Von-Ossietzky-Straße 99, 37085 Göttingen, Germany

L. Wegewitz · W. Maus-Friedrichs
Clausthaler Zentrum für Materialtechnik, Technische Universität Clausthal, Leibnizstrasse 4, 38678 Clausthal-Zellerfeld, Germany

F. Qi · A. P. Weber
Institut für Mechanische Verfahrenstechnik, Technische Universität Clausthal, Leibnizstrasse 19, 38678 Clausthal-Zellerfeld, Germany

Introduction

Titanium dioxide in the form of anatase shows high catalytic activity for degradation of organic compounds under UV light. However, anatase is the low temperature crystal form. Upon heating over 400 °C it will transform in rutile, which is the thermostable and inactive form of titanium dioxide. That limits the applications of titanium dioxide at high temperature processes and the phase stabilization of anatase is therefore of major interest. Qi et al. [1] have observed that the thermostability of anatas was enhanced up to 1,000 °C with silicon dioxide coating in a flame synthesis reactor. The SiO_2 coating was performed in the same flame as the TiO_2 nanoparticle formation by adding the precursor $SiCl_4$ at a distance from the nozzle where the formation of the Titania nanoparticles was already completed. However, when calcinating the coated particles later at temperatures above 900 °C, a part of the anatase nanoparticles transformed into the rutile phase because of the inhomogenenity of the amorhpous silica layers on the titania particles. Okada et al. [2] have investigated the effect of silica additives on the anatase-to-rutile phase transition in liquid phase and concluded that an amorphous silicon layer on titania nanoparticles is important in retarding the anatase-to-rutile transition by suppressing diffusion between anatase particles in direct contact and limiting their ability to act as surface nucleation site for rutile. Since, in contrast to liquid based techniques, the gas phase synthesis enables the production of high purity nanoparticles at high throughputs a generic process for uniform coatings is highly desired. Therefore, this contribution explores the feasibility of plasma coating processes which may be coupled with different nanoparticles synthesis techniques operated in the gas phase.

Plasma treatments with silane containing process gases for means of film deposition has been investigated for a long time with regard to various applications. The critical issue for all of the techniques published so far is to avoid the silane from contact to oxygen, since this would precipitate this precursor [3]. Especially for the deposition of oxide films, this is quite challenging, since oxygen is required for the deposition process. Recently, several approaches are made to deal with this task. One approach is to use elaborate streaming processes, e.g. capillary jet injection [4], or helicon diffusion setup [5]. The other approach is to either employ more complex metal–organic precursors as gaseous siloxanes [6, 7], or to use other oxygen sources, e.g. CO_2 or N_2O [8–14]. The elaborate streaming approaches on the one hand require complex setups and are difficult to integrate into industrial processing chains. On the other hand, changing either one of the precursors, SiH_4 or O_2 towards more complex molecules leads to residual contents of these changed precursors to remain in the deposited films, such as carbon or nitrogen [15, 16].

While there is a large number of publications available dealing with investigations on titanium dioxide by means of surface science, especially X-ray photoelectron spectroscopy (XPS), most of these studies deal with adsorption and chemistry. Publications providing a full disclosure of binding energies or chemical shifts and full widths at half maximum (FWHM) for the elements Ti and O are rare [17]. Furthermore, many of the reported values for binding energies, chemical shifts, etc. are contradictory to some extend [17]. These may be due to several difficulties in quantitative interpretation of the XPS results of titanium compounds. Since some of the chemical species in complex Ti–O–N compounds are only separated in binding energy by about 0.2 eV, this is far beyond the resolution reachable with commercial X-ray sources. The background is difficult to subtract due to reasonable inelastic scattering, which gets even more complicated due to intense shake up satellites at some 13 eV above the main peaks [18]. The main structure used for detailed chemical analysis of titanium compounds is the Ti 2p, since it is the most pronounced structure of

the titanium spectrum. Unfortunately, the line widths for Ti $2p_{3/2}$ and Ti $2p_{1/2}$ differ due to a different Coster-Kronig broadening, just alike most transition metals [18–21]. In addition to that, the peak areas ratio of the Ti $2p_{3/2}$ compared to the Ti $2p_{1/2}$ is commonly assumed to be 2:1, or even reported to be larger [18], while it should be 1.94 :1 when taking into account the two different photo-ionization cross sections [22]. The binding energies have been evaluated from literature very detailed in our previous publication while investigating the interaction of titanium surfaces with different plasma discharges [23]. These binding energy values are summarized in Table 1.

Many studies specify the binding energy for the O 1s peak belonging to TiO_2 [24–29] very similarly, within just a small standard deviation of 0.37 eV. Thus, the average of all of these binding energy values, which calculates to 529.9 eV has been used to discuss the recent results later on in this manuscript. The binding energy of a Ti–O–N intermediate species for the O 1s peak has been reported to amount to 531.3 eV independently by several investigations [24, 27]. The binding energy of adsorbed OH groups has been evaluated through various references before to amount to 531.8 eV as has been described in detailed within a previous publication [23]. The N 1s structure of titanium oxynitride films can contain several pure and oxidized nitrogen states, which have been accounted according to [23]. All O 1s and N 1s values from reference data have been summarized in Table 2.

The band bending [30] and charging effects [17, 31–33] tend to become rather large on TiO_2 surfaces. Thus, the application of absolute binding energies seems to be inappropriate when fitting experimental data due to the uncertainty of the binding energy shift induced by band bending and surface charging. Some of the literature data is recorded with the experimental setup for charge compensation either by binding energy correction along to structures of some gold coating [27], or by electron dosage using a flood gun just until the adventitious carbon peak is found according to given literature [17, 34]. In contrast to these approaches, taking into account relative binding energies between all species found instead of absolute values should always lead to a reasonable interpretation of experimental data.

Table 1 Literature values of binding energy, chemical shift and doublet splitting for the Ti 2p structure of Ti–O-N—compounds in XPS [23]

Peak	Tetrahedron	Bonding unit	Binding energy/eV	Chemical shift/eV
Ti $2p_{3/2}$	Ti–Ti$_4$	Ti	453.9	0.00
	Ti–Ti$_2$H$_2$	TiH	454.1	0.20
	Ti–Ti$_3$O	Ti$_2$O	454.2	1.10
	Ti–Ti$_2$O$_2$	TiO	455.3	1.35
	Ti–N$_4$	TiN	455.5	1.55
	Ti–TiO$_3$	Ti$_2$O$_3$	457.1	3.20
	Ti–O$_x$N$_{4-x}$	TiO$_x$N$_y$	457.1	3.15
	Ti–O$_4$	Ti(OH)$_4$	457.1	3.20
	Ti–O$_4$	TiO$_2$ amorph	458.7	4.80

Peak	Tetrahedron	Bonding unit	Binding energy/eV	Doublet splitting/eV
Ti $2p_{1/2}$	Ti–Ti$_4$	Ti	460.0	6.13
	Ti–Ti$_2$O$_2$	TiO	461.0	5.73
	Ti–TiO$_3$	Ti$_2$O$_3$	462.7	5.60
	Ti–O$_4$	TiO$_2$ amorph	464.4	5.66

Table 2 Literature values of binding energy and chemical shift for the O 1s and N 1s structures of Ti–O–N—compounds in XPS [23]

Peak	Bonding unit	Binding energy/eV	Chemical shift/eV
O 1s	TiO_2	529.9	0.00
	TiO_xN_{4-x}	531.3	1.40
	$Ti(OH)_4$	531.8	1.90

Peak	Bonding unit or state	Binding energy/eV	Chemical shift/eV
N 1s	β-N	396.0	−0.60
	TiN	396.6	0.00
	α-N_2	397.3	0.65
	CN_x	400.0	3.40
	γ-N	400.0	3.40
	NO_2	403.5	6.90
	N_2O_4 (NO_2-Dimer)	406.0	9.40
	NO_3	407.0	10.40

Amongst the given references, the authors tried to collect a consistent set of values necessary for reasonable interpretation and reproducible quantitative analysis of the XPS spectra of titanium oxynitrides. Basing on values supported by most papers as reviewed by Biesinger et al. [17], data from charge corrected measurements on reference samples as opposed to DFT calculations have been adjoined. Reference data have been completed by values averaged from independent investigations of several applied samples where standard deviations are satisfyingly small. The fitting procedures presented later on are based on these results, i.e. the chemical shifts as well as binding energy differences between different atoms for the bonding units presented above. The evaluated binding energy differences as summarized in Tables 1 and 2 have been successfully used before on different plasma treated titania samples [23].

The literature reporting on silicon oxides, silicon nitrides and mixtures of both compounds is quite divided about binding energies and chemical shifts for XPS. From a large number of references, a set of binding energy values has been selected, just similar to evaluation with regard to the titanium compounds presented above. The binding energy values and chemical shifts of the Si 2p and the O 1s for the silicon oxides have been gathered from Himpsel et al. and Sutherland et al. [35, 36] Both were employing synchrotron radiation for sufficient resolution, while charging effects were minimized through oxide film thicknesses. The chemical shifts and relative binding energies of the Si 2p for the silicon nitrides have been taken from Choo et al. [37], who investigated nitrogen terminated silicon nanoparticles. Even though the measurements on these nanoparticles might have been influenced by charging effects, this would not have any impact on relative energies and shifts. The N 1s binding energies for the silicon nitrides have been identified from combined theoretical methods and experiments by Rignanese et al. [38]. The Si 2p core level energy for the precursor molecule SiH_4 has been taken from data tables by Jolly et al. [39]. All binding energy differences evaluated from the given references are summarized in Tables 2 and 3.

The tetrahedron notation used in Tables 1, 2, 3 and 4 as well as during the discussion of our recent results is implemented analogous to the notation of Cova et al. [34] for silicon oxynitride films. Since there are several bonds inducing equal oxidation states at the titanium

Table 3 Literature values of binding energy and chemical shift for the Si 2p structure of Si–O–N—compounds in XPS

Peak	Tetrahedron	Bonding unit	Binding energy/eV	Chemical shift/eV	References
Si 2p	Si–Si$_4$	Si	98.3	0.00	35
	Si–Si$_3$O	Si$_2$O	99.3	0.95	35
	Si–Si$_3$N	Si$_3$N	99.5	1.20	37
	Si–Si$_2$O$_2$	SiO	100.1	1.75	35
	Si–Si$_2$N$_2$	Si$_3$N$_2$	100.7	2.40	37
	Si–SiO$_3$	Si$_2$O$_3$	100.8	2.48	35
	Si–SiN$_3$	SiN	101.8	3.50	37
	Si–O$_4$	SiO$_2$	102.2	3.90	36
	Si–N$_4$	Si$_3$N$_4$	103.3	5.00	37
	Si–H$_4$	SiH$_4$	107.3	9.00	39

Table 4 Literature values of binding energy and chemical shift for the O 1s and N 1s structures of Si–O–N—compounds in XPS

Peak	Tetrahedron	Bonding unit	Binding energy/eV	Chemical shift/eV	References
O 1s	O–Si$_2$	SiO$_2$	532.2		36
N 1s	N–Si$_3$	Si$_3$N$_4$	397.8	0.00	36
	N–Si$_2$O$_1$	(H$_3$SiO)N(SiH$_3$)$_2$	399.6	1.77	38
	N–Si$_1$O$_2$	(H$_3$SiO)$_2$N(SiH$_3$)	401.6	3.78	38
	N–O$_3$	(H$_3$SiO)$_3$N	403.4	5.55	38

atoms, the notation of oxidation states is not unique and thus not capable for discussions. The different models that are commonly used to describe the structure of amorphous nonstoichiometric alloys are the random bonding model (RBM) and the random mixture model (RMM) [40–43]. According to silicon-centered tetrahedrons considered by Cova et al. the discussion of titanium species will be held considering titanium-centered tetrahedrons. Silicon films grown by low pressure chemical vapor deposition techniques have been found difficult to analyze with the strict models RBM and RMM. Thus, a more general model has been proposed to be useful especially for films grown under highly nonequilibrium conditions, e.g. plasma-assisted chemical vapor deposition techniques. The new approach proposed by Cova et al. the extended random mixture model (ERMM) demands a well choice of the most adequate tetrahedral structures among all possible candidates. After exclusion of unlikely tetrahedrons, the remaining units have to be considered during the numerical fitting of XPS spectra, using binding energies gained through calculations as well as reference spectra of pure standard samples. Finally, the fractions of the total number of atoms belonging to that species can be calculated taking into account the stoichiometry coefficient for the species related to the particular tetrahedron [40].

Experimental Details

An ultra high vacuum apparatus with a base pressure of 5×10^{-11} hPa is used to carry out the experiments [44]. All measurements were performed at room temperature.

Electron spectroscopy is performed using a hemispherical analyzer (VSW HA100) in combination with a source for metastable helium atoms (mainly He* $^3S_1$) and ultraviolet photons (HeI line). A commercial non-monochromatic X-ray source (Specs RQ20/38C) is utilized for XPS.

During XPS, X-ray photons irradiate the surface under an angle of 80° to the surface normal, illuminating a spot with a diameter of several mm. For all measurements presented here the Al K_α line (photon energy 1,486.6 eV) is used. Electrons are recorded by the hemispherical analyzer with an energy resolution of 1.1 eV emitted under an angle of 10° to the surface normal. All XPS spectra are displayed as a function of binding energy with respect to the Fermi level.

For quantitative XPS analysis, photoelectron peak areas are calculated via mathematical fitting with Gauss-type profiles using OriginPro 7G including the PFM fitting module, which applies Levenberg–Marquardt algorithms to achieve the best agreement possible between experimental data and fit. To optimize our fitting procedure, Voigt-profiles have been applied to various oxidic and metallic systems previously, but for most systems the Lorentzian contribution converges to zero. Therefore, all XPS peaks are fitted with Gaussian shapes. The background correction was done by the combination of a Shirley-type background correction with the high binding energy site limit at the maximum of the first shake up satellite and a subsequent linear subtraction. Although it has been shown that constant tail background approaches yield best results, its advantage is negligible due to the lack of pure standard spectra [18]. Photoelectric cross sections as calculated by Scofield [22] with asymmetry factors after Powell and Jablonski [45], taking into account asymmetry parameters after Reilman et al. [46] and Jablonski [47] as well as inelastic mean free paths from the NIST database [48] (using the database of Tanuma, Powell and Penn for elementary contributions and the TPP-2 M equation for molecules) as well as the energy dependent transmission function of our hemispherical analyzer are taken into account when calculating stoichiometries. All film thickness evaluations have been done from XPS results via attenuation of the Ti 2p peak employing the intermediate mean free path (IMFP) in the film, the angle θ between the surface and the direction of electron detection and the peak intensities I_0 before and I_d after film deposition using the formula [49]:

$$d = \text{IMFP} \cdot \cos \theta \cdot \ln \left[\frac{I_0}{I_d} \right].$$

Plasma treatments have been carried out employing a dielectric barrier discharge. The plasma source is mounted to a preparation chamber with a base pressure of 5×10^{-8} hPa which is connected directly to the UHV recipient via a common transfer system and has been described elsewhere [50]. An alternating high voltage pulse generator with a pulse duration of 0.6 μs and a pulse repetition rate of 10 kHz is connected to the dielectric isolated electrode, while the sample forms the grounded counter electrode. The discharge gap is set to about 1 mm and the discharge area is about 2 cm^2. During the plasma treatment, a voltage of 11 kV (peak) is measured. The high voltage supply delivers a power of 2 W, the plasma power density can be calculated to 1 W/cm^2 and with a plasma treatment time of 60 s, an energy density of 60 J/cm^2 is applied to the sample The increase of the sample temperature during the plasma treatment does not exceed 10 K [51].

Silane (Linde Gas, 1.5 at% in 98.5 at% N$_2$), O$_2$ (Linde Gas, 99.995 %) and ambient atmospheric air are offered via backfilling the chamber using a bakeable leak valve. The gas line is evacuated and can be heated in order to ensure cleanness. A quadrupole mass

spectrometer (Balzers QMS 112 A) is used to monitor the partial pressure of the reactive gases simultaneously during all experiments. The titanium dioxide nanoparticles (Degussa P25, 99.5 % TiO_2, average diameter 21 nm) are deposited onto a molybdenum washer as suspension in ethanol, which is afterwards evaporated.

The topography of the TiO_2 particles prior to and after the plasma treatments is determined by Atomic Force Microscopy (AFM) using a Veeco Dimension 3100 SPM. All measurements are performed in Tapping Mode with Al-coated silicon cantilevers (NSC15, Micromasch). The typical resonance frequencies of this series are about 325 kHz, typical spring constants are in the range of 40 N/m. The radius of the tip curvature is less than 10 nm. All images consist of 512 lines each containing 512 pixels. They are recorded with a line-scan frequency of 0.5 Hz. SPIP (Image Metrology A/S) is used for the depiction of the AFM images and the calculation of the average surface roughness (RMS) according to ISO 4287/1.

Results and Discussion

The results on the plasma based silicon dioxide coating are presented in two parts. First, the TiO_2 substrate is cleaned by heating up to 600 °C prior to the SiH_4/N_2 plasma treatment, followed by an O_2 plasma treatment. In the second part, the substrate is plasma treated in SiH_4/N_2 as prepared with all atmospheric adsorbates at the surface and afterwards oxidized by a plasma treatment in atmospheric air.

Plasma Treatment of Cleaned TiO_2 Powders in SiH_4/N_2 and O_2

Figure 1 shows the XPS spectra of (from left to right) the C 1s, Ti 2p, O 1s, Si 2p and N 1s regions of a cleaned TiO_2 powder sample (black lines and squares, top spectra), after the SiH_4/N_2 plasma treatment (red lines and triangles, middle spectra) and after the subsequent O_2 plasma treatment (green lines and diamonds, bottom spectra). The samples were cleaned by heating up to 600 °C, the Ti 2p and O 1s regions resemble a stoichiometric TiO_2 very well. Even though some residual carbon remains, most adsorbants have been removed by the cleaning procedure.

After the plasma treatment in the gaseous mixture of SiH_4 and O_2, the intensities of the Ti 2p and O 1s structures are severely reduced due to the deposited overlayer. The intensity of the C 1s decreases less than that of the Ti 2p and O 1s peaks, indicating some kind of distribution of the carbon through the adsorbed film. The Ti 2p region clearly reveals a second state at the low binding energy side of the original Gaussians, which corresponds to Ti–TiO_3 (Ti_2O_3) according to the literature values for the chemical shifts (see Table 1). After the plasma treatment, Si 2p and N 1s structures are found. The N 1s region reveals only one peak, corresponding to nitrides. Since small amounts of oxygen have been found to inhibit the formation of titanium nitrides during plasma treatments [23], all nitrogen is assumed to be bound at the adsorbed silicon, which is supported by the absence of any sign of nitrides or oxynitrides in the Ti 2p region. The O 1s structure also reveals a second peak after the plasma treatment, which might correspond to some compound of the adsorbed silicon. The amount of this second O 1s peak is rather small compared to the N 1s intensity, thus any silicon oxides are neglected in the analysis. The Si 2p region is displayed together with the resulting Gaussians for Si–Si_3N, Si–Si_2N_2, Si–SiN_3 and Si–N_4 (corresponding to Si_3N, Si_3N_2, SiN and Si_3N_4). Even though the resolution of the spectrometer does not allow a certain discrimination between these
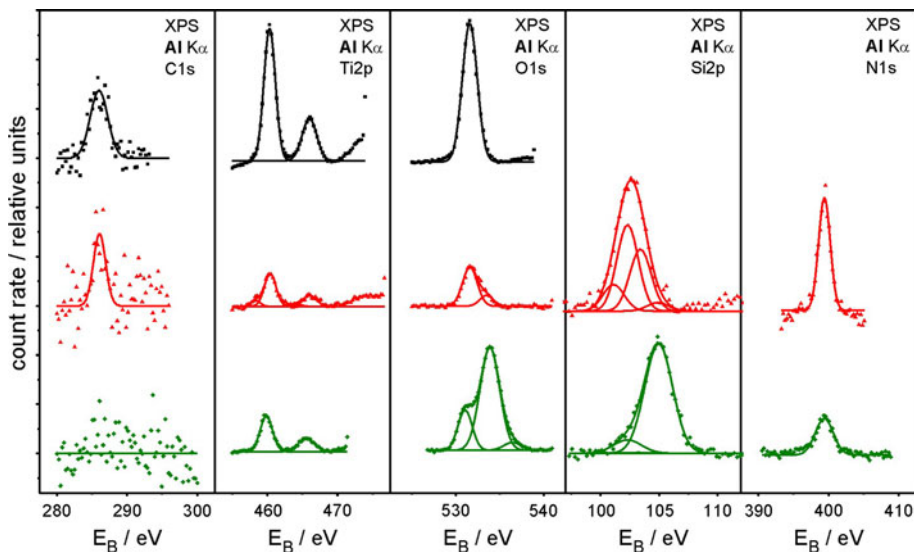
Fig. 1 XPS spectra of the C 1s, Ti 2p, O 1s, N 1s and Si 2p regions of the cleaned TiO_2 powder (*black lines* and *squares, top spectra*), after SiH_4/N_2—plasma treatment (*red lines* and *triangles, middle spectra*) and after subsequent O_2—plasma treatment (*green lines* and *diamonds, bottom spectra*) (Color figure online)

species, the N 1s peak appears to determine the position of these peaks very well, employing the binding energy differences from Tables 3 and 4. Furthermore, the assumption of a negligible amount of oxynitrides is strongly suggested by the absence of any surplus N 1s species. Taking all this into account, the absolute fractions of the four species suffer from the described variances. Nevertheless, the fit results qualitatively reveal the existence of at least all silicon nitride compounds in the deposited film. The silicon nitride film thickness calculation via attenuation of the Ti 2p peak yields about 3.1 nm.

The subsequent O_2 plasma treatment nearly eliminates the C 1s peak, while the nitrogen concentration is reduced to about one-third. The Ti 2p region again shows only the peaks corresponding to stoichiometric TiO_2. The O 1s structure shows a significant increase of the second peak, indicating its correlation to silicon oxides. An additional third peak appears in the O 1s region after O_2 plasma treatment, which is most probably due to OH groups adsorbed after the plasma treatment from some residual water in the O_2 gas. The Si 2p region now consists mainly of one peak at the binding energy position of SiO_2 relative to the corresponding O 1s peak. The second peak at the low binding energy side is at the position of $Si-Si_2N_2$, but the obvious broadening indicates some remaining $Si-Si_3N$ and $Si-SiN_3$, too. Nevertheless, the silicon nitride fraction is remarkably reduced. The film thickness of the silicon oxynitride layer slightly increases up to 3.7 nm.

Figure 2 depicts the AFM images of an untreated TiO_2 powder sample (a) and the cleaned TiO_2 powder sample after consecutive treatments in silane/nitrogen and pure oxygen (b). In the image of the cleaned powder several discrete particles can be discovered despite the strong agglomeration which shows up in most regions of the picture. The average diameter of the untreated particles is about 22 ± 3 nm which is in good agreement with the manufacturer information. The RMS roughness of the surface amounts to 13.3 nm. The average diameter of the particles after the plasma treatments amounts to 31 ± 6 nm, indicating an overlayer thickness of approximately $3 - 7$ nm in comparison to the aforementioned diameter of 22 nm. The RMS roughness is slightly smaller (12.1 nm),
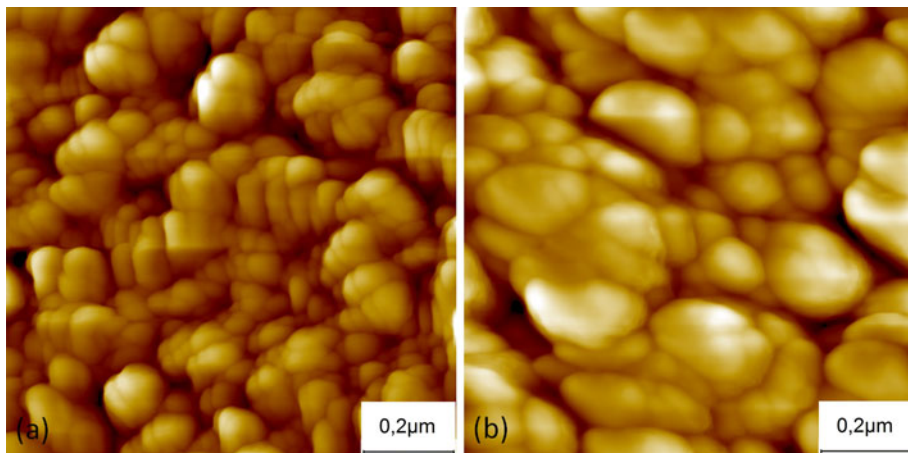
Fig. 2 AFM images of an untreated TiO_2 powder sample (**a**, *left image*) and the cleaned TiO_2 powder sample after SiH_4/N_2—plasma treatment and subsequent O_2—plasma treatment (**b**, *right image*), the image areas are $1 \times 1 \ \mu m^2$

but the basic structure with several distinct particles and huge areas of agglomerates is preserved.

The two step film deposition process employing a plasma treatment in a gaseous mixture of 1.5 % SiH_4 and 98.5 % N_2 followed by a plasma treatment in pure oxygen has been shown to grow a film consisting of mainly silicon dioxide. The increase in film thickness by the second plasma can be explained by the different lattice constants. The final film thickness estimated by peak attenuation in XPS is in good agreement to the standard deviation of the augmentation of the particle diameter. The transformation of the initially grown silicon nitride has progressed considerably with only about 5 % residual Si_3N_4 molecules within the film.

Plasma Treatment of as Prepared TiO_2 Powders in SiH_4/N_2 and Air

Figure 3 shows the XPS spectra of (from left to right) the C 1s, Ti 2p, O 1s, Si 2p and N 1s regions of a TiO_2 powder sample as prepared (black lines and squares, top spectra), after SiH_4/N_2 plasma treatment (red lines and triangles, middle spectra) and after the subsequent air plasma treatment (green lines and diamonds, bottom spectra). The untreated powder sample yields only the Ti–O4 structures in the Ti 2p region, while the O 1s regions shows a main feature corresponding to titanium oxides as well as a surplus peak at higher binding energies corresponding to atmospheric surface adsorbates. The C 1s region shows a broadened structure due to the various adsorbates, which seems to consist of at least two peaks. The peak at lower binding energies may be corresponding to atomic carbon, whereas the peak at higher binding energies represents carbon oxides [52].

After the SiH_4/N_2 plasma treatment, the Ti 2p intensity decreases due to the deposited overlayer, again, while in this case no surplus peaks appear, indicating no plasma-induced reduction of the TiO_2 surface. The Si 2p region again reveals a variety of silicon nitrides to be present in the just deposited film. Again, the single N 1s peak as well as the absence of any surplus peaks in the O 1s region suggest that no oxynitrides have been formed. The C 1s peaks does not decrease as much as the Ti 2p and O 1s peaks, thus indicating some
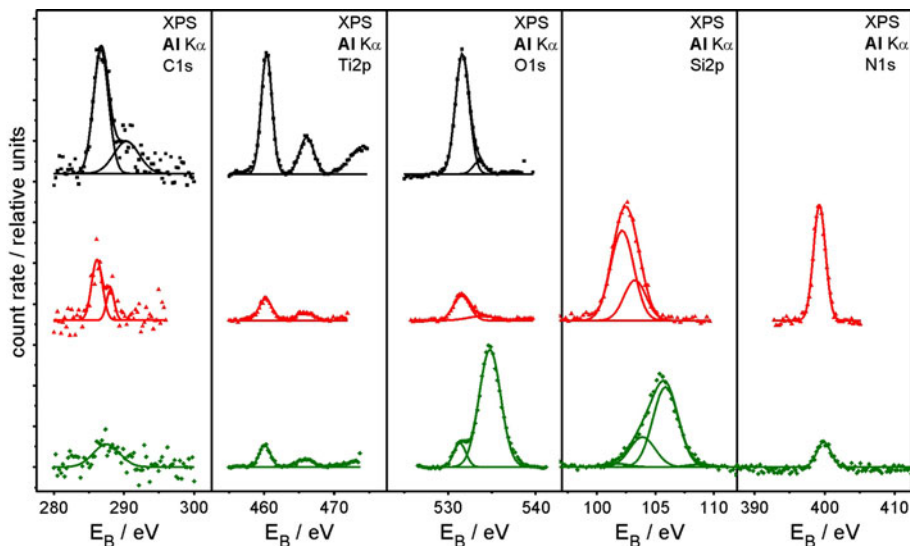
Fig. 3 XPS spectra of the Ti 2p, O 1s, C 1s, N 1s and Si 2p regions of the TiO$_2$ powder as prepared (*black lines* and *squares*), after SiH$_4$/N$_2$—plasma treatment (*red lines* and *triangles*) and after subsequent air—plasma treatment (*green lines* and *diamonds*) (Color figure online)

kind of distribution through the deposited film, again. The attenuation of the Ti 2p signal yields a silicon nitride film thickness of about 3.7 nm.

The subsequent air plasma leads to an increase in the Ti 2p intensity, indicating the corresponding decrease in the thickness of the deposited film. The O 1s region shows a very large new peak, that can be assigned to the silicon oxides, while the peak due to adsorbates is gone. The C 1s and N 1s intensities are significantly decreased and the two C 1s peaks can not be distinguished any more. The Si 2p region shows two additional peaks at higher binding energies that can be assigned to mainly Si–O$_4$, while the peak at highest binding energies can not be correlated to any oxide, nitride or oxynitride species. The thickness of the silicon oxynitride film is considerably increased and now amounts to about 4.9 nm.

In Fig. 4, AFM images of the untreated TiO$_2$ powder sample (a) and the uncleaned powder sample after the process combination of silane/nitrogen plasma followed by air plasma treatment (b) are depicted. The surface exhibits large agglomerates of TiO$_2$ particles. Only a few distinct particles could be identified, which explains the considerably larger deviation range of the average particle diameter of 35 ± 7 nm. The RMS roughness of the surface amounts to 16.5 nm and is therefore considerably larger compared to the oxygen treated sample. The increase in the particle size indicates an overlayer thickness of 4 − 10 nm.

The silicon nitride film deposition process via a plasma treatment in a gaseous mixture of 1.5 % SiH$_4$ and 98.5 % N$_2$ on as-prepared TiO$_2$ powders yields a notably larger film thickness compared to the cleaned powders. This may be caused by the surplus oxygen and carbon species introduced into the film by the molecules initially adsorbed on the surface. The subsequent air plasma treatment has been shown to transform the silicon nitride film very effectively into a silicon oxide film. In this case, the final film thickness estimated by peak attenuation in XPS is quite well within the standard deviation of the augmentation of
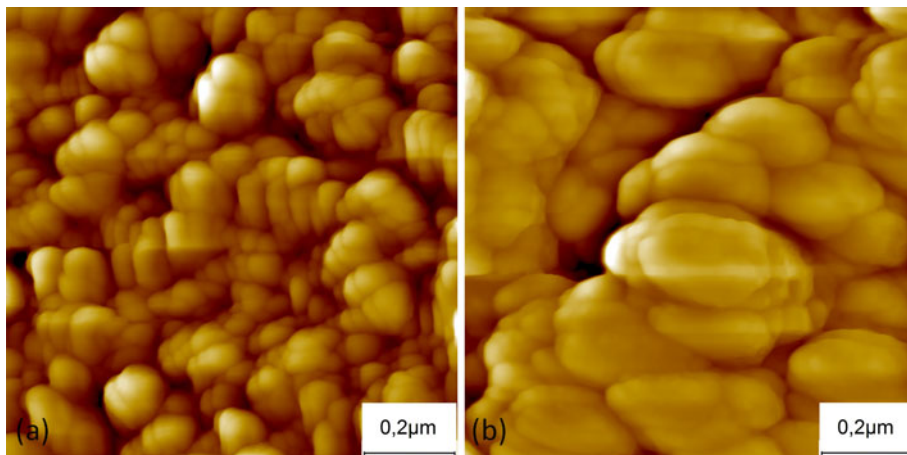
Fig. 4 AFM images of an untreated TiO_2 powder sample (**a**, *left image*) and the uncleaned TiO_2 powder sample after SiH_4/N_2—plasma treatment and subsequent air—plasma treatment (**b**, *right image*), the image area is 1×1 μm^2

the particle diameter. The residual content of Si_3N_4 molecules in the film after the air plasma treatment amounts to about 3 %, which means the transformation of the initial grown silicon nitride has progressed even better than for the oxygen plasma on the TiO_2 powders cleaned prior to the SiH_4/N_2 plasma treatment (Tables 5, 6).

Comparison of Both Film Deposition Pathways

Figure 5 shows the process scheme of the experiments above. Comparing the results from Sections "Plasma Treatment of Cleaned TiO_2 Powders in SiH_4/N_2 and O_2" and "Plasma Treatment of as Prepared TiO_2 Powders in SiH_4/N_2 and Air", it seems to be unnecessary to clean the surface of the particles from atmospheric adsorbates in a separate process step before the film deposition. The nitrogen content of the SiH_4/N_2 process gas has been shown to remove all oxygen containing contaminations, while the remaining carbon got mostly removed by the subsequent oxidizing plasma. The predominance of the nitrogen molecules in the air plasma treatment did not have any negative effect on the conversion of the silicon nitride into silicon oxide. Indeed, the air plasma treatment at 1,000 mbar seems to be much more effective than the oxygen plasma treatment at 200 mbar, while the oxygen partial pressures were comparable. This enhancement may originate in an increased generation of the reactive oxygen species via a deexcitation path of the nitrogen as described by Trompeter et al. and Penetrante et al. [53, 54]. Nevertheless, both deposition pathways have been shown to produce smooth silicon oxide films with negligible amounts of residual silicon nitride, whereas no influence on the titanium dioxide particles took place. All film thicknesses, oxide ratios and nitride fractions have been summarized in Table 7.

Summary

The coating of titanium dioxide nanoparticles with a silicon dioxide film has been performed by means of plasma treatment employing silane as gaseous precursor. In contrast to

Table 5 XPS results for the cleaned TiO_2 powder sample upon SiH_4/N_2—and subsequent O_2—plasma treatment

System	Peak	Species	Binding energy/eV	FWHM/ eV	Relative fraction	Stoichiometry (%)
Cleaned TiO_2	C 1s	Interfacial	286.0	2.98	1.00	3.2
	O 1s	TiO_2	531.6	2.00	1.00	69.3
	Ti 2p$_{3/2}$	TiO_2	460.3	1.94	1.00	27.5
	Ti 2p$_{1/2}$	TiO_2	466.0	2.46	1.00	
After SiH_4–plasma	C 1s	Interfacial	286.3	2.05	1.00	2.8
	N 1s	Si_3N_4	399.4	1.97	1.00	16.10
	O 1s	TiO_2	531.6	1.96	0.80	28.2
		OH (ads)	533.5	1.79	0.20	
	Si 2p	Si_3N	101.1	2.14	0.14	43.8
		Si_3N_2	102.3	2.14	0.47	
		SiN	103.4	2.14	0.34	
		Si_3N_4	104.9	2.14	0.05	
	Ti 2p$_{3/2}$	Ti_2O_3	458.4	0.12	0.12	9.1
		TiO_2	460.2	0.88	0.88	
	Ti 2p$_{1/2}$	Ti_2O_3	464.0	0.16	0.16	
		TiO_2	465.9	0.84	0.84	
After subsequent O_2-plasma	C 1s	Interfacial	–	–	–	0.0
	N 1s	Si_3N_4	399.4	3.04	1.00	5.0
	O 1s	TiO_2	531.1	1.90	0.21	65.7
		SiO_2	533.9	2.62	0.74	
		OH (ads.)	536.4	2.31	0.05	
	Si 2p	Si_3N_2	102.3	2.81	0.11	23.7
		SiN	103.4	2.81	0.01	
		Si_3N_4	104.9	2.81	0.00	
		SiO_2	105.0	2.81	0.89	
	Ti 2p$_{3/2}$	TiO_2	459.9	2.07	1.00	5.7
	Ti 2p$_{1/2}$	TiO_2	465.6	2.80	1.00	

existing techniques that use pure silane [5, 14], silane diluted in hydrogen [14, 55, 56] or silane diluted in noble gases [57–59], the described process bases on a nitrogen gas with only 1.5 % silane content. Thus, the easy handling of this process gas allows a cheap and simple implementation even for industrial application. The silicon nitride film resulting from this process gas has afterwards been converted into silicon dioxide by means of an oxygen or air plasma. While the oxygen supply is one of the critical points in all existing techniques for SiO_2 film deposition from silane precursors, the whole process is simplified by splitting the deposition and the oxidations into two steps. Furthermore, the combination of these two plasma treatments cleans the nanoparticles surfaces during the deposition process from all atmospheric contaminants or adsorbants. Best results for clean film deposition were gained on nanoparticles that have not been cleaned prior to the deposition process and using atmospheric air for the oxidation step, despite all possible contamination sources.

🅐 Springer

Table 6 XPS results for the as prepared TiO_2 powder sample upon SiH_4/N_2—and subsequent air—plasma treatment

| System	Peak	Species	Binding energy/eV	FWHM/ eV	Relative fraction	Stoichiometry (%)
As-prepared TiO_2	C 1s	C–C, C–H	286.7	2.55	0.70	15.4
		C–O	290.3	4.23	0.30	
	O 1s	TiO_2	531.6	1.87	0.92	61.2
		OH (ads.)	533.5	1.61	0.08	
	Ti $2p_{3/2}$	TiO_2	460.4	1.83	1.00	23.4
	Ti $2p_{1/2}$	TiO_2	466.1	2.41	1.00	
After SiH_4-plasma	C 1s	C–C, C–H	286.1	1.81	0.73	5.9
		C–O	288.1	1.31	0.27	
	N 1s	Si_3N_4	399.3	2.04	1.00	20.1
	O 1s	TiO_2	531.6	2.21	0.76	20.6
		SiO_2	533.9	3.94	0.24	
	Si 2p	Si_3N_2	102.2	2.34	0.70	46.5
		SiN	103.3	2.20	0.30	
	Ti $2p_{3/2}$	TiO_2	460.2	2.24	1.00	6.0
	Ti $2p_{1/2}$	TiO_2	465.8	2.94	1.00	
After subsequent air-plasma	C 1s	Interfacial	287.5	4.42	1.00	2.3
	N 1s	Si_3N_4	399.9	2.35	1.00	3.0
	O 1s	TiO_2	531.3	1.64	1.00	63.9
	Si 2p	Si_3N	101.6	2.56	0.03	27.8
		Si_3N_2	102.8	2.56	0.00	
		SiN	103.9	2.56	0.26	
		Si_3N_4	105.4	2.56	0.00	
		SiO_2	105.9	2.56	0.69	
		–	109.4	2.56	0.02	
	Ti $2p_{3/2}$	TiO_2	460.1	1.89	1.00	3.0
	Ti $2p_{1/2}$	TiO_2	465.9	2.92	1.00	
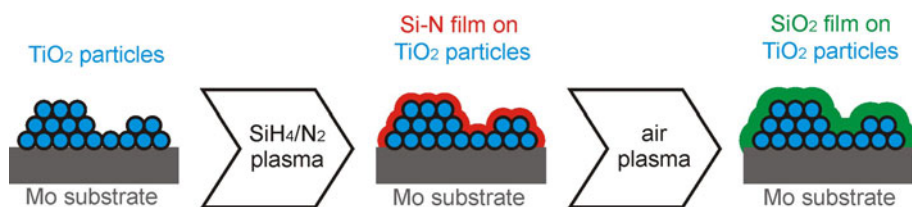
Fig. 5 Process scheme of the proposed two-step film deposition technique employing the combination of a SiH_4/N_2 plasma and an air plasma

The application of the presented process includes the coating of individual particles inside a system of two particle flow reactors. Therefore, dispersed nanoparticles will be carried by the gaseous flow through a system of two similar plasma reactors that will be subject of a prospective project.

Table 7 Summarized film thicknesses and oxygen/metal ratios

System	Si–O–N overlayer thickness	O over Si+Ti ratio	Nitride fraction
Heated TiO$_2$ powder	–	2.52	0.00
+SiH$_4$/N$_2$ plasma	3.14	0.53	*1.00*
+O$_2$ plasma	3.69	2.23	0.03
Untreated TiO$_2$ powder	–	2.61	0.00
+SiH$_4$/N$_2$ plasma	3.73	0.39	*1.00*
+Air plasma	4.88	2.08	0.05

References

1. Qi F, Moiseev A, Deubener A, Weber AP (2011) J Nanopart Res 13:1325–1334
2. Okada K, Yamamoto N, Kameshima Y, Yasumori A, MacKenzie KJD (2001) J Am Ceram Soc 84:1591–1596
3. Cho JH, Lin I (1993) J Appl Phys 74:4741–4745
4. Botha R, Haj Ibrahim B, Bulkin P, Drevillon B (2008) J Vac Sci Technol A 26:1115
5. Charles C, Boswell RW (1997) J Appl Phys 81:43–49
6. Coclite AM, Milella A, Palumbo F, Fracassi F, d'Agostino R (2009) Plasma Process Polym 6:512–520
7. Navamathavan R, Jung AS, Kim CY, Choi CK, Lee HJ (2008) J Korean Phys Soc 53:1468–1474
8. Mukhpadhyay S, Ray S (2011) Appl Surf Sci 257:9717–9723
9. Nakamura K, Yamaguchi Y, Ykokyama K, Higashida K, Ohmi H, Kakiuchi H, Yasutake K (2011) J Nanosci Nanotechnol 11:2851–2855
10. Dao VA, Nguyen VD, Heo J, Choi H, Kim Y, Lakshminarayan N, Yi J (2009) Vacuum 84:410–414
11. Boogaard A, Kovalgin AY, Brunets I, Aarnink AAI, Holleman J, Wolters RAM, Schmitz J (2007) Surf Coat Technol 201:8976–8980
12. Shi G, Xu G, Han G (2007) Mater Lett 61:463–465
13. da Silva Zambom L, Verdonck P (2006) Thin Solid Films 515:596–598
14. Samanta A, Das D (2009) Sol Energy Mater Sol C 93:588–596
15. Boudreau M, Boumerzoug M, Mascher P, Jessop PE (1993) Appl Phys Lett 63:3014–3016
16. Wrobel AM, Blaszczyk-Lezak I, Uznanski P, Glebocki B (2010) Chem Vap Depos 16:211–215
17. Biesinger MC, Lau LWM, Gerson AR, Smart R, St C (2010) Appl Surf Sci 257:887–898
18. Robinson KS, Sherwood PMA (1984) Surf Interface Anal 6:261–266
19. de Siervo A, Landers R, de Castro SGC, Kleiman GG (1998) J Electron Spectr Relat Phenom 88–91:429–433
20. Nyholm R, Martensson N, Lebugle A, Axelsson U (1981) J Phys F Metal Phys 11:1727–1733
21. Yarzhemsky VG, Reich T, Chernysheva LV (1992) J Electron Spectr Relat Phenom 58:67–73
22. Scofield JH (1976) J Electron Spectrosc Relat Phenom 8:129–137
23. Dahle S, Gustus R, Viöl W, Maus-Friedrichs W (2012) Plasma Chem Plasma Process 32:1109–1125. doi:10.1007/s11090-012-9392-x
24. Rodriguez JA, Jirsak T, Liu G, Hrbek J, Dvorak J, Maiti A (2001) J Am Chem Soc 123:9597–9605
25. Cheung SH, Nachimuthu P, Joly AG, Engelhard MH, Bowman MK, Chambers SA (2007) Surf Sci 601:1754–1762
26. Chen X, Lou Y, Samia ACS, Burda C, Gole JL (2005) Adv Funct Mater 15:41–49
27. Prokes SM, Gole JL, Chen X, Burda C, Carlos WE (2005) Adv Funct Mater 15:161–167
28. Xu J, Ao Y, Fu D, Yuan C (2008) J Cryst Growth 310:4319–4324
29. Fàbrega C, Andreu T, Güell T, Prades JD, Estradé S, Rebled JM, Peiró F, Morante JR (2011) Nanotechnology 22:235403
30. Campbell CT (1997) Surf Sci Rep 27:1–111
31. McCafferty E, Wightman JP (1999) Appl Surf Sci 143:92–100
32. Massaro C, Rotolo P, De Riccardis F, Milella E, Napoli A, Wieland M, Textor M, Spencor ND, Brunette DM (2002) J Mater Sci Mater Med 13:535–548

33. Hashimoto S, Tanaka A, Murata A, Sukarada T (2004) Surf Sci 556:22–32
34. Cova P, Poulin S, Grenier O, Masut RA (2005) J Appl Phys 97:073518
35. Himpsel FJ, McFeely FR, Taleb-Ibrahimi A, Yarmoff JA (1988) Phys Rev B 38:6084–6096
36. Sutherland DGJ, Akatsu H, Copel M, Himpsel FJ, Callcott TA, Carlisle JA, Ederer DL, Jia JJ, Jimenez I, Perera R, Shuh DK, Terminello LJ, Tong WM (1995) J Appl Phys 78:6761–6769
37. Choo C-K, Sakamoto T, Tanaka K, Nakata R (1999) Appl Surf Sci 148:116–125
38. Rignanese G-M, Pasquarello A, Charlier J-C, Gonze X, Car R (1997) Phys Rev Lett 79:5174–5177
39. Jolly WL, Bomben KD, Eyermann CJ (1984) Atom Data Nucl Data 31:433–493
40. Gritsenko VA, Kwok RWM, Wong H, Xu JB (2002) J Non-Cryst Solids 297:96–101
41. Sassella A (1993) Phys Rev B 48:14208–14215
42. Hasegawa S, He L, Inokuma T, Kurata Y (1992) Phys Rev B 46:12478–12484
43. Yin Z, Smith FW (1990) Phys Rev B 42:3658–3665
44. Frerichs M, Voigts F, Maus-Friedrichs W (2006) Appl Surf Sci 253:950–958
45. Powell C, Jablonski A (2010) J Electron Spectrosc Relat Phenom 178:331–346
46. Reilman RF, Msezane A, Manson ST (1976) J Electron Spectrosc Relat Phenom 8:389–394
47. Jablonski A (1995) Surf Interface Anal 23:29–37
48. National Institute of Standards and Technology Electron Inelastic-Mean-Free-Path Database 1.2, http://www.nist.gov/srd/nist71.cfm. Accessed 29 Feb 2012
49. Ertl G, Küppers J (1985) Low energy electrons and surface chemistry. VCH Verlag, Weinheim
50. Wegewitz L, Dahle S, Höfft O, Voigts F, Viöl W, Endres F, Maus-Friedrichs W (2011) J Appl Phys 110:033302
51. Kogelschatz U (2003) Plasma Chem Plasma Phys 23:1–46
52. Chen L, Chen F, Shi Y, Zhang J (2012) J Phys Chem C 116:8579–8586
53. Trompeter FJ (2001) PHD thesis at the RWTH Aachen
54. Penetrante BM, Hsiao MC, Bardsley JN, Merritt BT, Vogtlin GE, Kuthi A, Burkhart CP, Bayless JR (1997) Plasma Sources Sci Technol 6:251–259
55. Müllerova J, Sutta P, van Elzakker G, Zeman M, Mikula M (2008) Appl Surf Sci 254:3690–3695
56. Nunomura S, Kondo M (2009) J Phys D Appl Phys 42:185210
57. Raha D, Das D (2008) J Phys D Appl Phys 41:085303
58. Kovalgin AY, Isai G, Holleman J, Schmitz J (2008) J Electrochem Soc 155:G21–G28
59. Wang D, Liu Q, Li F, Qin Y, Liu D, Tang Z, Peng S, He D (2010) Appl Surf Sci 257:1342–1346